Surfaces and Interfaces 40 (2023) 103090

Contents lists available at ScienceDirect

Surfaces and Interfaces

journal homepage: www.sciencedirect.com/journal/surfaces-and-interfaces

Nanomechanical surface properties of co-sputtered thin film polymorphic metallic glasses based on Ti-Fe-Cu, Zr-Fe-Al, and Zr-W-Cu

C.R. Onyeagba [a,c,d,*], M. Valashani [a,c,d], H. Wang [b,c,d], C. Brown [a,c,d], P. Yarlagadda [c,d,e], T. Tesfamichael [a,c,d]

[a] School of Mechanical, Medical and Process Engineering, Faculty of Engineering, Queensland University of Technology, Brisbane, QLD 4000, Australia
[b] School of Chemistry and Physics, Faculty of Science, Queensland University of Technology, Brisbane, QLD 4000, Australia
[c] Centre for Biomedical Technologies, Queensland University of Technology, Brisbane, QLD 4000, Australia
[d] Centre for Materials Science, Queensland University of Technology, Brisbane, QLD 4000, Australia
[e] School of Engineering,University of Southern Queensland, Springfield Central, QLD 4300

ARTICLE INFO

Keywords:
Co-sputtering
Metallic glass
Nanostructured thin films
Nanomechanical
Coatings

ABSTRACT

Metallic glasses are amorphous materials that have shown prospects in several applications including biomedical due to their superior and unique mechanical, tribological, and bioactive properties. New functional coatings of thin film polymorphic metallic glasses (Ti-Fe-Cu, Zr-Fe-Al, and Zr-W-Cu) were deposited by co-sputtering of constituents from high purity (99.9%) targets. The thin film metallic glasses were deposited on stainless steel 316 L (SS316L) and titanium alloy (Ti) substrates. Co-sputtering offers tuneable parameters (pressure, power, and time), which fosters high-quality polymorphic films of desired thickness and composition. Surface and nanomechanical properties of the films, including surface morphology, structure, mechanical, and tribological properties were investigated using SEM, AFM, XRD, XPS, nanoindentation, and scratch test. The coated substrates exhibit uniform nanostructured films with surface roughness in the range of 1.5 to 7 nm. The XRD spectra show a dominant amorphous glassy polymorphic feature on both substrates with crystallites size in the range of 65–108 nm. Nanomechanical characteristics of the films suggest high wear resistance with film adhesion strength ranging between 624 - 2159 μN and 2273 - 2978 μN on SS316L and Ti substrates, respectively. Overall, these polymorphic Ti-Fe-Cu, Zr-Fe-Al, and Zr-W-Cu nanostructured uniform films with low surface roughness and high adhesion on SS316L and Ti substrates are potential functional surfaces for biomedical applications.

1. Introduction

The need for a mechanically robust protective surface coating to resist wear, corrosion, and even bacterial proliferation continues to grow by the day. The engineering field has seen great evolution of materials and processes for critical applications. For example, nanostructured metallic materials such as titanium [1,2], silver, copper, zinc, etc. [3,4] have been reported to kill bacterial [5,6]. However, their bactericidal efficacy tends to diminish with time due to corrosion, wear and mechanical robustness of the nanostructure surface [7–9].

Bulk Metallic glasses (BMGs) are potential candidates for advanced applications due to their mechanical robustness, enhanced corrosion and wear resistance which emanates from their amorphous phase [10]. In the past two decades BMGs have been produced based on Zr, Au, Fe, Pt, Cu, Mg, and Ti [11,12], in conjunction with other elements of high glass-forming ability [13]. Zr-based BMGs and Ti-based BMGs have both excellent mechanical properties and corrosion resistance. BMGs have been used as orthopaedic and dental device materials, such as implanted pins, screws, plates, nails, and dental implants [14]. Orthopaedic and dental device materials are needed to survive in a harsh human body environment for a long time. One of the problems of the current BMGs, the limited diameter sizes restrain the design and types of biomedical devices using BMGs [15,16]. One promising measure to solve the limited components size of BMGs is a thin film form of Zr-based and Ti-based BMGs [14]. The other problem of BMGs is the localization of deformation within shear bands reporting a brittle-like failure behaviour [17]. Kazuhiro Imai [18] also suggest that MGs as thin films onto the substrate of biomedical devices can be a solution as the deformation

* Corresponding author at: School of Mechanical, Medical and Process Engineering, Faculty of Engineering, Queensland University of Technology, Brisbane, QLD 4000, Australia.
E-mail addresses: chijiokeraphael.onyeagba@hdr.qut.edu.au (C.R. Onyeagba), t.tesfamichael@qut.edu.au (T. Tesfamichael).

https://doi.org/10.1016/j.surfin.2023.103090
Received 27 January 2023; Received in revised form 8 June 2023; Accepted 17 June 2023
Available online 23 June 2023

mechanism of BMGs under compression, bending and cycle loading gradually changes from brittle to ductile as thickness decreases from bulk to sub-microns [19–22] due to lower shear band displacement.

Sputtering is an industry-viable PVD system with tuneable parameters that fosters development of nanostructured thin film MGs by co-deposition [12,23]. Zr-based thin film MGs have been reported to have an improved mechanical and tribological properties [24], because of geometrical confinement (short grain boundary conditions) and the introduction of a crystalline phase [25], that have attracted much interest in sporting equipment (golf clubs, tennis, etc.) cell phone cases, spaceships, and medical devices [26]. Ti-based thin film MGs have also been reported to exhibit good wear resistance [27] and excellent biocompatibility [28] that are critical in biomedical and medical devices.

Moreover, recent studies show that, ductility of MGs could be improved by admixing a smaller proportion ($< 50\%$) of crystalline phase (i.e. polymorphous metallic glasses) [17]. Polymorphous thin film metallic glasses (PTFMG) have not been reported extensively. Nanostructured PTFMG are a new class of MGs that could foster innovative properties beneficial in several industries.

This work presents the surface and nanomechanical properties of new Ti- and Zr-based nanostructured PTFMG fabricated by co-sputtering on 316 L stainless steel (SS316L) and Titanium (Ti) substrates. X-ray Diffractometer (XRD) was used to determine the thin films' glassy amorphous and polymorphic phases. X-ray photoelectron spectroscopy (XPS) was used to obtain the elemental, composition and stoichiometry of the films in accordance with the procedure suggested by Greczynski [29]. To support the XPS elemental results, EDS measurements were performed. Surface morphology, roughness, and microstructure of the films on each substrate were measured by atomic force microscopy (AFM) and Field emission scanning electron microscope (FESEM). Dynamic nanoindentation and nano-scratch examination were performed to analyse the mechanical and tribological behaviour of the thin films as the techniques have proven to be reliable for investigating surface hardness, fracture toughness, stiffness and elastic modulus [30]. Depth profiling dynamic nanoindentation test gives a much better estimation of the elastic properties of the thin films compared to the quasi-static indentation test. This is because the properties obtained from a quasi-static test are usually affected by the properties of the substrate, following the 10% rule of film thickness [31,32]. A shallow indentation depth is also not ideal, as the film roughness can affect the properties [32,33]. A solution to this problem is to obtain the storage modulus and hardness as a function of indentation depth following the standard test method outlined in ISO 14,577–4 [33,34], and to eliminate substrate effect and get a good estimate of the Young's modulus and hardness, a common practice is to linearly extrapolate storage modulus and hardness to vanishing contact depth [35]. Nano-scratch also provides good tribology information [36,37]. The point at which the coating begins to fail, break, or delaminate from the substrate (i.e., adhesive failure) is known as the critical load (L_c). L_c is also described as the stress required to remove a coating from a substrate [24] which can be regarded as the adhesive strength of the film and in our study, this is the critical lateral force (*Lf*). The variation of *Lf* on each substrate with individual ramping loads; normal force (*Nf*) was examined in tandem with the deformation behaviour of the film/substrate system. FESEM was used to observe the deformation behaviour of the film. The film adhesion was discussed as a measure of the *Lf* and FESEM observations.

2. Experimental procedure

2.1. Ti- and Zr-based thin film deposition

KJ Lesker PVD 75 magnetron sputtering system with 4 target sources of 50 mm diameter was employed to deposit Ti- and Zr-based PTFMG samples on SS316L stainless steel and polished Ti substrates. Details of the PVD system and several trail samples on glass, stainless steel and polished Ti substrates are shown in the supplementary document. Before film deposition, the substrates were cleaned with distilled water and dried with an air gun. Sputtering target materials of Ti, Zr, Fe, Cu, W, Al, Mg, Ta, Hf purchased from Maideli Advanced Material Co., Ltd were selected based on their glass-forming ability, including incompatibility of crystal structure and atomic size of the alloying elements [38], and biocompatibility. The purity level of the sputtering targets was between 99.95% and 99.99%. To successfully obtain PTFMGs, three element combination (Table S1 and S2 supplementary document) were selected from the target materials based on their incompatible crystal structures (BCC, FCC and HCP) and a co-sputtering principle (cluster + glue atom model) [39,40], where the cluster is the base element (Ti-based or Zr-based) and glue atoms are supplementary elements (Fe, Cu, W, Al, Mg, Ta, Hf). Consequently, the cluster is major constituent of the admixture and should have higher deposition power than the glue atoms.

Deposition power of 150 W for the cluster target (Ti or Zr) and 50 W for the corresponding glue supplementary elements at working pressure of 10 mTorr and sputtering time of 60 min were applied. To maintain uniformity of the films, the substrate was rotated at 10 rpm. The substrate holder was fixed at a distance of 150 mm from the target and no heating was applied to the substrate. The chamber was pumped for vacuum environment until desired base pressure was achieved ($< 2.0 \times 10^{-6}$ mTorr), followed by introduction of pure argon for processing. The targets were pre-sputtered for 5 min to remove surface contaminants followed by film deposition onto the substrates. Based on greatest polymorphous composition ($> 50\%$ amorphous) and microstructural uniformity of the films, one Ti-based and two Zr-based samples (Ti-Fe-Cu: Sample ID 3; Zr-Fe-Al: Sample ID 5; and Zr-W-Cu: Sample ID 7) were selected amongst the several samples shown in Table S2 for further investigation (see Table 1). It is important to note that the film stoichiometry, thickness and polymorphous composition (amorphous/crystalline ratio) are a function of the deposition parameters, thus not predefined. Consequently, the properties of the films in Table 1 are not reported optimal values. Moreover, the substrates (SS316L and Ti) of different roughness (14 nm and 4 nm) were chosen to obtain a surface costing with the suggested range of roughness (< 10 nm) for effective nanostructures bactericidal surfaces [41,42].

2.2. Ti- and Zr-based thin film characterization

The thickness of the films on glass substrate was measured using DektakXT-Bruker stylus profilometer. A SCANASYST in air-Dimension Icon (BRUKER) AFM operated in semi-contact mode with Silicon Nitride cantilevers was used to characterize the surface morphology and roughness of the films. FESEM (JOEL 7001F) with an acceleration voltage of 5 kV was used to investigate the surface and microstructure of the samples. Grazing incidence XRD measurements were performed using Rikagu X-ray Diffractometer - powder high throughput, thin film, Cu/Mo Smartlab to obtain the polymorphous (amorphous/crystalline) composition of the films.

The chemical composition and stoichiometry of the thin films were studied using X-ray photoelectron spectroscopy (XPS) using a Kratos

Table 1
Film compositions, thickness, and roughness (Ra) of the co-sputtered nanostructured polymorphous thin film metallic glass samples on SS316L and Ti substrates. Note that the surface roughness of SS316L and polished Ti bare substrates are 14 nm and 4 nm, respectively.

Sample ID	Film stoichiometry	Thickness (nm)	Roughness (nm) on each substrate	
			SS316L	Ti
3	$Ti_{47}Fe_{41}Cu_{12}$	190	7	3
5	$Zr_{71}Fe_{3}Al_{26}$	298	3	2
7	$Zr_{58}W_{31}Cu_{11}$	280	2	1.5

Axis Supra with aluminium monochromatized Al Kα X-ray radiation (hν = 1486.7 eV). analyser pass energy of 160 eV was used for wide survey scans, and a pass-energy of 20 eV was utilized for high-resolution scans of the O 1 s and Mo 3d regions to differentiate the sub-structure of the spectral lines effectively. The spectra were acquired sequentially with incidence angle of the gas cluster ion beam at an angle of 45° normal to the sample. The size of the analysed sample area was 300 × 600 μm with 10 min per scan acquisition time. It is important to note the analysis was done on several random areas (at least 3) on the sample surfaces for affirmation of the compositions. After analysis, a 2 mm × 2 mm area of the samples were sputter-etched for 60 s with 10 keV Ar1000+ to confirm C and O are surface contaminants. Additionally, XPS measurements of the samples were carried out without the charge neutralizer to check for any shift or charging. Further experimental procedures are described in detail in the supplementary document. For the quantification, the CasaXPS© software version 2.3.19 PR1.0 was used with the appropriate element sensitivity library for the Kratos instrument. All peaks were fitted using a Shirley background, by using a 70% Gaussian/30% Lorentzian peak shape.

EDS measurements were performed using Oxford Aztec STD X-act. Versatility and high resolution across the magnification range of 5X - 300,000X of the JOEL 7001F to confirm the elemental composition of the bulk.

The nanomechanical properties of the nanostructured PTFMG on SS316L and Ti substrates were examined using a Hysitron TI 950 nanoindenter, with a Berkovich tip (radius 150 nm). The tip area function of the Berkovich indenter was carefully calibrated on the fused quartz with known reduced modulus (69.6 GPa ± 5%) and hardness (9.3 GPa ± 10%). Continuous dynamic test (CMX method with peak load 10,000 μN) can measure the mechanical property X (i.e., Young's modulus and hardness) continuously while indenting into the material to get its depth profile. This was conducted on the samples with respect to the film thickness (190 nm, 280 nm, and 298 nm) to obtain accurate properties of the films. This was done under constant strain rate of 0.05 s^{-1}. Five sections of nine indents were performed on random areas (at least 100 μm apart) of the film surface to obtain accurate undeniable results. The dimension of each sample is 12 mm × 12 mm.

The tribology (wear resistance, fracture toughness, and film/substrate adhesion) of the samples were examined at different structural states based on the cooperative shear model theory [43]. Nano-scratch tests were carried out to evaluate the shear and wear resistance of the PTFMG. Three pair scratches were performed at several areas on individually coated substrates, with a space interval of 2 to 3 μm to obtain the mean critical loads with ramping load from 0 to 2000 μN, 0 to 3000 μN, and 0 to 5000 μN. This technique involves generating a controlled scratch with a sharp diamond tip on a selected area. The sharp diamond tip is used to induce a controlled scratch on the film surface under the constant progressive load of 0.05 nm/s speed. The penetration depth of the triboindenter diamond tip during scratching is a function of elastic and plastic deformations of the individual PTFMG on SS316L and Ti substrates [44]. The ramping load schemes were used to create 10 μm scratch tracks. The tip was cleaned by performing an array of indents on aluminium before and after each scratch to avoid effect of residual chips. The length and the scratch tracks were examined under FESEM to observe the plastic behaviour.

3. Results and discussion

The nanomechanical, tribological and surface properties, including composition, phase, morphology, stoichiometry, and film thickness of Ti- and Zr-based samples are discussed. As shown in Table 1, the thickness and surface roughness of the PTFMGs were all under 300 nm and 10 nm, respectively. As expected, the films are generally rougher on the SS316L substrate than the polished Ti substrate due to the higher surface roughness of the bare SS316L (14 nm for SS316L and 4 nm for polished Ti).

3.1. Film properties

Fig. 1 shows XPS spectra of the Ti- and Zr-based PTFMG samples on SS316L and Ti substrates. The analyses show that the samples contain C, O, alongside the Ti-Fe-Cu, Zr-Fe-Al, and Zr-W-Cu. The C and O are surface contaminants adsorbed from the atmosphere, and no trace of these elements was observed after lightly etching the films. EDS spectra (see Fig. S3 in the supplementary document) confirms the elemental composition of the films. Due to the bulk effect of EDS, the substrates were detected in the EDS spectra as shown in Fig. S3. Therefore, the stoichiometry and composition of the three films were extracted from XPS as shown in Table 1.

Fig. 2 shows the high resolution XPS spectra of Ti 2p, Fe 2p, Cu 2p, Zr 3d, W 4f, and Al 2p for the co-sputtered Ti-Fe-Cu, Zr-Fe-Al, and Zr-W-Cu on SS316L and Ti substrates. All XPS spectra are charge referenced to the Fermi edge cut-off which is set at 0 eV in all valence band spectra (see **Fig. S5** of the supplementary document). The binding energies (BE) of O 1 s and C 1 s are set at 530.0 eV and 285 eV, respectively. The Zr 3d core level (see Fig. 2a) is located at approximately 182.2 eV and 184.6 eV that corresponds to ZrO_2 [45]. The W spectrum was separated into two spin–orbit doublet peaks (see Fig. 2b) corresponding to metallic and oxide of W. While the W $4f_{5/2}$ and W $4f_{7/2}$ peaks located at BE of 37.8 and 35.6 eV are ascribed to W^{6+}oxidation state, the W $4f_{5/2}$ and W $4f_{7/2}$ peaks at 33.0 and 31.0 eV are typical W metal [46,47].The Cu 2p core level (see Fig. 2c) spectrum was fitted at 932.6 eV, which is assigned to Cu (0) [48]. The Fe 2p core level (see Fig. 2d) was fitted at 710 eV from the main Fe 2p3/2 peak which reflects Fe-oxygen bond (oxidation state Fe^{3+}) [49,50]. The Al 2p core level spectrum (see Fig. 2e) has a main peak located at 72.1 eV, denoting the presence of metallic aluminium [51]. The Ti 2p core level spectrum (see Fig. 2f) was fitted with two peaks with BEs of 458.5 eV and 464.2 eV which corresponds to Ti 2p3/2 and Ti 2p1/2 respectively, denoting Ti-oxygen bond (oxidation state Ti^{4+}) [52,53].

Fig. 3 shows XRD pattern of Ti-Fe-Cu (a,b), Zr-Fe-Al (c.d) and Zr-W-Cu (e,f) PTFMG on SS316L and Ti substrates. The XRD pattern of the Ti-based (Ti-Fe-Cu) PTFMG shows a broad hump with about 55% amorphous characteristics on both substrates. Fe and Ti (Table 2) were identified as the major elements of the crystal phase (crystallites) on both substrates, respectively. This may be a substrate effect since Fe and Ti are constituents of the crystalline substrates (SS316 and Ti), respectively. The percentage of amorphous/crystalline characteristics of the polymorphic metallic glass thin films was deduced from the XRD software DIFFRAC.EVA V6 using the following equations:

$$\%\text{Amorphous} = \frac{\text{Global area} - \text{Reduced area}}{\text{Global area}} \times 100 \quad (1)$$

$$\%\ \text{Crystallinity} = 100 - \%\text{Amorphous} \quad (2)$$

The Zr-based (Zr-Fe-Al and Zr-W-Cu) PTFMGs, showed broad XRD spectra on SS316L and Ti substrates. Zr-Fe-Al (Fig. 3c,d) demonstrates polymorphic properties with amorphous (crystalline) phase proportion of 76% (24%) and 67% (33%) on SS316L and Ti substrates, respectively. Fe and Zr3Fe (Table 2) were identified as the primary contributor to the crystal phase (crystallites) on both substrates, respectively. The crystallite of Fe appears to be pronounced on the SS316L substrate for , which may be a joint effect of the presence of Fe in the film ternary and SS316L, thus, substrate effect. The XRD of Zr-W-Cu in (Fig. 3e,f) displays 72% (28%) and 74% (26%) of amorphous (crystalline) phase proportion on the SS316L and Ti substrates, respectively. Both Cu and W were identified as the crystallites on both substrates.

It is important to note that in addition to the glass forming ability, incompatibility of crystal structure (hexagonal close packing-HCP, body centred-BCC, face centred-FCC) and atomic size discourages vitrification and promote the formation of predominant amorphous phase [59]. In this study, the co-sputtered $Ti_{47}Fe_{41}Cu_{12}$, $Zr_{71}Fe_{3}Al_{26}$ and $Zr_{58}W_{31}Cu_{11}$ matrix featured from unique structure combination of HCP (Ti, Zr) - BCC

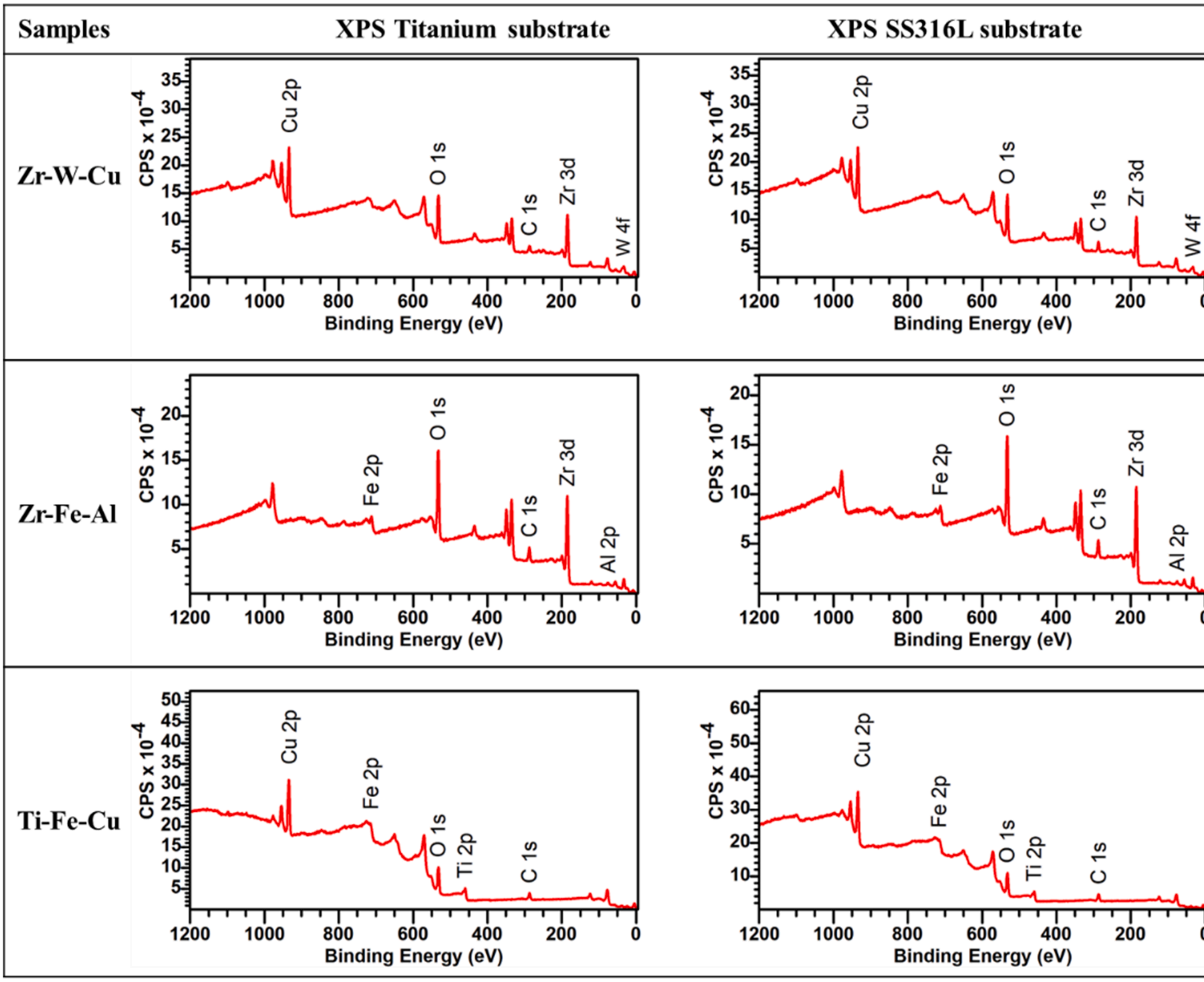

Fig. 1. XPS spectra of: (a) Zr-W-Cu, (b) Zr-Fe-Al, and (c) Ti-Fe-Cu nanostructured polymorphous thin films metallic glasses on SS316L and Ti substrates.

(Fe, W), and FCC (Al ,Cu). This combination also fosters high strength and stiffness (due to HCP and BCC) with good ductility (due to FCC) [60]. This will be substantiated by the nanomechanical test of the film reported in Section 3.2.

Fig. 4 shows AFM and FESEM images of the co-sputtered thin film MG samples (Ti-Fe-Cu, Zr-Fe-Al and Zr-W-Cu). The morphology of the films on the two substrates varies slightly with no visible crack or defect having AFM surface roughness ranging between 1.5 nm to 7 nm. This nanoscale roughness could benefit bactericidal efficacy, [42] and thus, a functional nanostructured surface coating. It is important to note that the higher roughness observed for the films on SS316L is because SS316L (14 nm) is rougher than polished Ti (4 nm) as mentioned earlier.

3.2. Nanomechanical and tribological properties

3.2.1. Modulus and hardness

As per depth profiling dynamic measurements, linear regression line-fitting (extrapolation) with zero intercepts on the y-axis (best-fit value of intercept = – 0.013 mN/nm) was used to estimate the elastic modulus and hardness of the films at shallow depths [61]. This was executed according to the testing standard (ISO 14,577–4) [34] which also corresponds to the elastic region and the maximum estimate of the indentation hardness as no plateau is observed [33]. Therefore, the film-only property was obtained. Please note that the loss modulus in our experiments was significantly smaller than the storage modulus. Therefore, the phase angle δ between the stress and strain is close to zero, and the elastic modulus that can be stated as $E = E'/\cos(\delta)$ is close to the reported storage modulus.

The hardness H is determined from the maximum load (Pmax) divided by the projected contact area (Ac):

$$H = Pmax/Ac \tag{3}$$

Five sections of nine indents were performed on random areas (at least 100 μm apart) of the film surface to obtain accurate undeniable results. Note that the area of the samples is 12 mm × 12 mm. The elastic modulus and hardness were estimated from the mean of four consistent indents over the film surface.

Table 3 shows the Young's modulus (*E*) and surface hardness (*H*) of the bare substrates, the Ti- and Zr-based metallic glasses. Generally, the bare SS316L and Ti substrates have higher Young's modulus [62,63], than the as-deposited PTFMGs (Table 3) which is beneficial to limit bone stress shielding [64]. Moreover, the PTFMG exhibit higher surface hardness (0.7 – 4.3 GPa) than bare SS316L (1.7 – 2.2 GPa) and Ti (3.3 – 3.7 GPa) [65–67], This affirms that surface coating could improve mechanical functionality of a material [68,69] especially with MGs. Also, the *E* and *H* values of the as-deposited PTFMGs are closely matched with

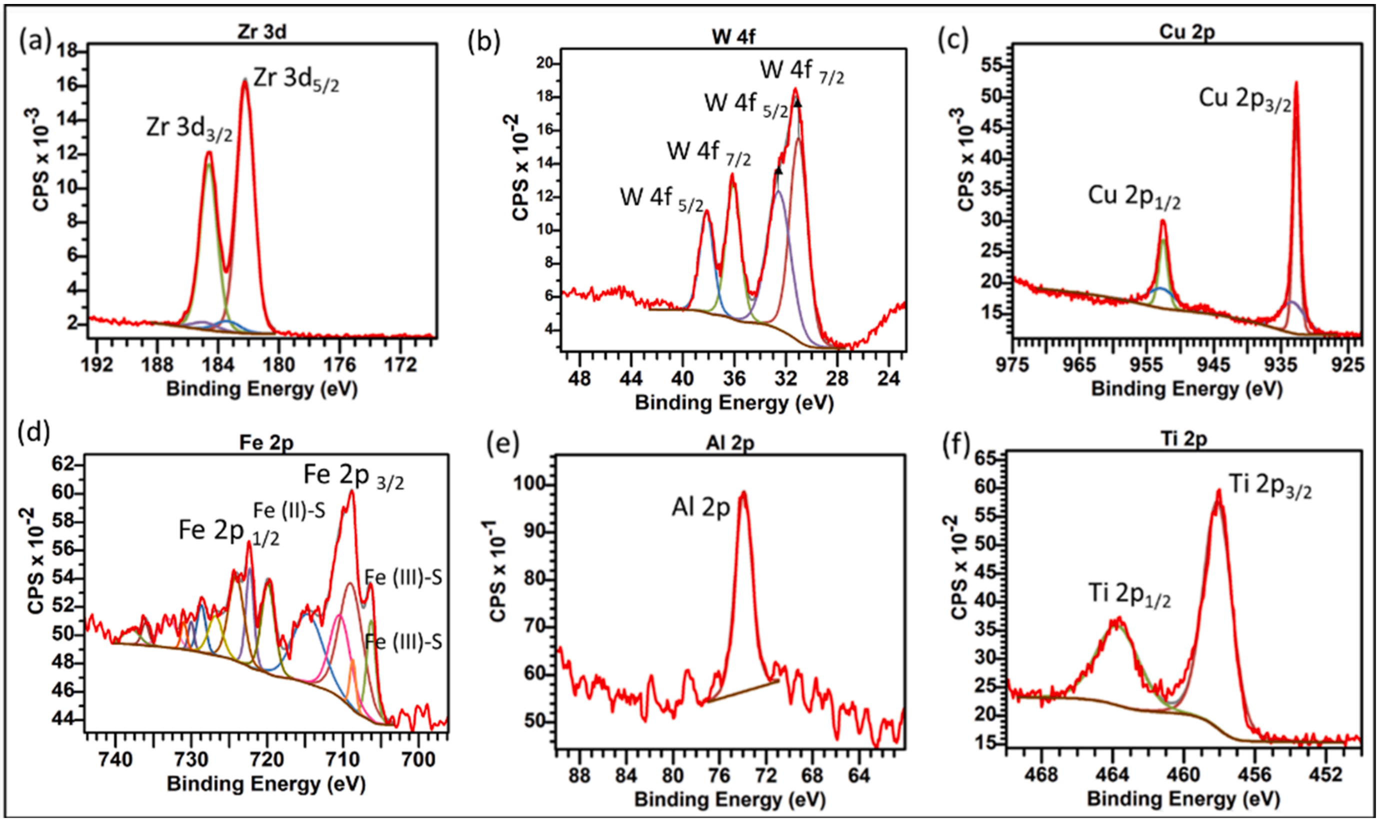

Fig. 2. Representative high resolution XPS spectra of (a) Zr 3d, (b) W 4f (c) Cu 2p (d) Fe 2p, (e) Al 2p, and (f) Ti 2p, for the co-sputtered Ti-Fe-Cu, Zr-Fe-Al, and Zr-W-Cu nanostructured polymorphous thin film metallic glass.

other studies; $Ti_{40}Zr_{10}Cu_{36}Pd_{14}$, $Zr_{46}Cu_{46}Al_8$, $Zr_{50}Cu_{50}$, and $Zr_{42}Cu_{42}Al_7Y_5$ (Table 3)

3.2.2. Ramping force nano-scratch (Tribology and wear)

The wear resistance, fracture toughness, and film/substrate adhesion properties of the as-deposited polymorphous thin film metallic glass is evaluated in this section as a function of lateral force (*Lf*) and lateral displacement (*dL*) with applied ramping force (N*f* ; 0 to 5000 μN) as shown in Table 4. A sudden increase (burst) in the lateral force (*Lf*) while performing a scratch at any ramping *Nf* section is a result of film failure/delamination [73]. If the hardness of the substrate is substantially greater than that of the film, the indenter exceeding the film thickness onto the substrate (substrate effect) with visual evidence can also be characterised by a burst [73]. The corresponding *Lf* (i.e. of the burst) is known as the adhesive strength of the film [74,24]. Moreover, where there is no burst, the corresponding *Lf* of the peak *Nf* (i.e. 5000 μN) without visible breakage or delamination from substrate as a function of lateral displacement (*dL*) and depth travelled also characterises film adhesive strength and fracture toughness.

According to Burnett and Rickerby's analysis, the film/substrate work of adhesion can be estimated to have a very high value of $1KJ/m^2$ from

$$L_c = \frac{\pi d_c^2}{8}\sqrt{\frac{2EW}{t}}, \tag{4}$$

where L_c is the critical load, d_c is the track width, E is the film's Young's modulus, t is the thickness of the film, and W is the work of adhesion [75].

The critical values of *Lf* (i, ii, iii) with corresponding *dL* at the individual ramping *Nf* for uncoated and coated substrates (see Table 4) are used to describe the film's tribology properties. These critical values are obtained for the bare and coated samples with the same nano-scratch conditions to characterise substrate effect/contact and thus, deduce film only property. Therefore, the tip of the indenter can be said to have reached the substrate at any of the scratch tracks when the *Lf* of the film ≥ *Lf* of the substrate at the corresponding *dL* of the substrate (see Table 4). This can be referred to as substrate contact. Beyond this point, the film/substrate bond is tested further as a function of shear strength. Except for Zr-Fe-Al deposited on SS316L, the indenter tip did not get to the substrate despite their film thicknesses (190 nm – 300 nm). This is due to their high strength and wear resistance.

It is important to note that the extended track characterised by white rectangular boxes seen in Figs. 4-7 are mainly on the last scratch tracks (5000 μN) results from the instrument's limitation at or beyond *Lf* 2000 μN. Hence, the graph represents only a 10 μm normal distance corresponding to the scratch tracks, excluding the boxed area.

Fig. 5 represents the nano-scratch patterns (tracks with corresponding graphs) of the bare substrates as a standard/control to understand substrate effects and estimate the tribology of the PTFMG-coated substrates. The peak lateral force (*Lf*) with the corresponding lateral displacement (*dL*) at the individual ramping *Nf* as shown in Table 4 is the reference for substrate effect/contact on the PTFMG-coated samples. The progression of the *Lf* on the bare substrates indicates more opposition to ramping on SS316L than on polished pure Ti.

Moreover, wider and shallow tracks are seen on SS316L as there was no recovery from the tip-induced deformation after unloading. On the other hand, deep and narrow tracks are observed on Ti as the material recovered from the tip-induced deformation after unloading. This demonstrates that SS316L and pure Ti are hard/strong substrates with a large plastic and elastic region respectively, the impact of these attributes on the co-sputtered PTFMGs is displayed by the FESEM micrograph of the individual samples on SS316L and Ti substrates.

Fig. 6 represents the *Lf* patterns (tracks with corresponding graphs) of nano-scratched Ti-Fe-Cu PTFMG on SS316L and Ti substrates for *Nf*

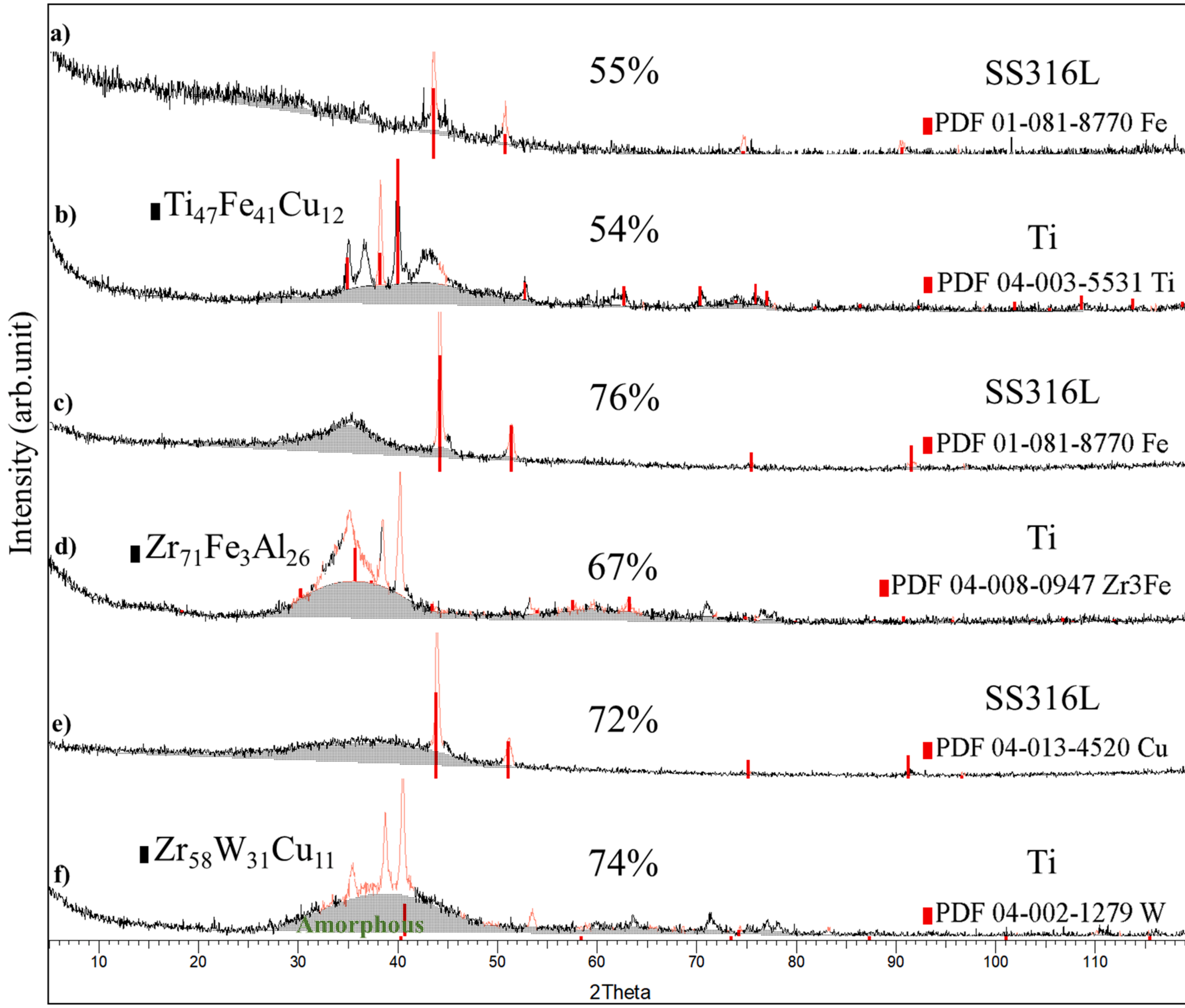

Fig. 3. XRD patterns with PDF crystal phase positions and amorphous% of the as-sputtered; (a,b) Ti-Fe-Cu, (c,d) Zr-Fe-Al, and (e,f) Zr-W-Cu PTFMGs on SS316L and Ti substrates.

Table 2
Size of the crystallites for the identified crystalline phases and the corresponding PDF card number with database reference to describe the polymorphous phase of the PTFMGs.

Sample	Substrate	Crystallites size (nm)	PDF card number	Ref
Ti-Fe-Cu	SS316L	82	01–081–8770 Fe	[54]
	Ti	108	04–003–5531 Ti	[55]
Zr-Fe-Al	SS316L	97	01–081–8770 Fe	[54]
	Ti	94	04–008–0947 Zr3Fe	[56]
Zr-W-Cu	SS316L	65	04–013–4520 Cu	[57]
	Ti	85	04–002–1279 W	[58]

2000, 3000, and 5000 μN. The Ti-Fe-Cu PTFMG shows excellent adhesion and fracture toughness on both substrates. Moreover, the *Lf* of the SS316L coated substrate is lower than on the Ti substrate (1921 μN < 2629 μN see Table 4) though more material is eroded off the Ti substrate. This is due to higher surface hardness (2.9 GPa for SS316L and 0.7 for Ti), thus resistance to penetration on SS316L than Ti. Furthermore, the ability of the film to resist breakage and delamination from the substrates is due to good film/substrate adhesion with large plastic and elastic region. This depicts high strength, wear and shear resistance [18].

Additionally, it is essential to note that substrate was not reached at any of the scratch tracks on the film with reference to Table 4 (Ti-Fe-Cu-coated SS316L *Lf* 1921 μN, *dL*8.9 μm and Ti *Lf* 2629 μN, *dL*8.5 μm compared to bare SS316L *Lf* 2554 μN, *dL*8.6 μm and Ti *Lf* 3014 μN, *dL*8.3 μm), which further affirms high strength, wear, and fracture resistance. This is a resultant effect of dense atom packing and the amorphous/crystalline phase of Ti-Fe-Cu PTFMG which emanates from the unique ternary combination of cubic structure (HCP, BCC, and FCC). This ternary Ti-Fe-Cu exhibits higher strength compared to other Ti-based MGs such as $Ti_{40}Zr_{10}Cu_{36}Pd_{14}$ (2100 μN) [76]. Ti-Fe-Cu has shown a potential for sustainable surface coatings that can endure progressive *Nf* up to 5000 μN.

Fig. 7 represents the *Lf* patterns (tracks with corresponding graphs) of nano-scratched Zr-Fe-Al PTFMG on SS316L and Ti substrates for *Nf* 2000, 3000, and 5000 μN. The film has relatively good adhesion, and fracture toughness on Ti substrate as high *Lf* with no breakage or delamination is observed at any point. On the other hand, beyond 4.1 *dL* of the last scratch track, brittle fracture followed by delamination of the

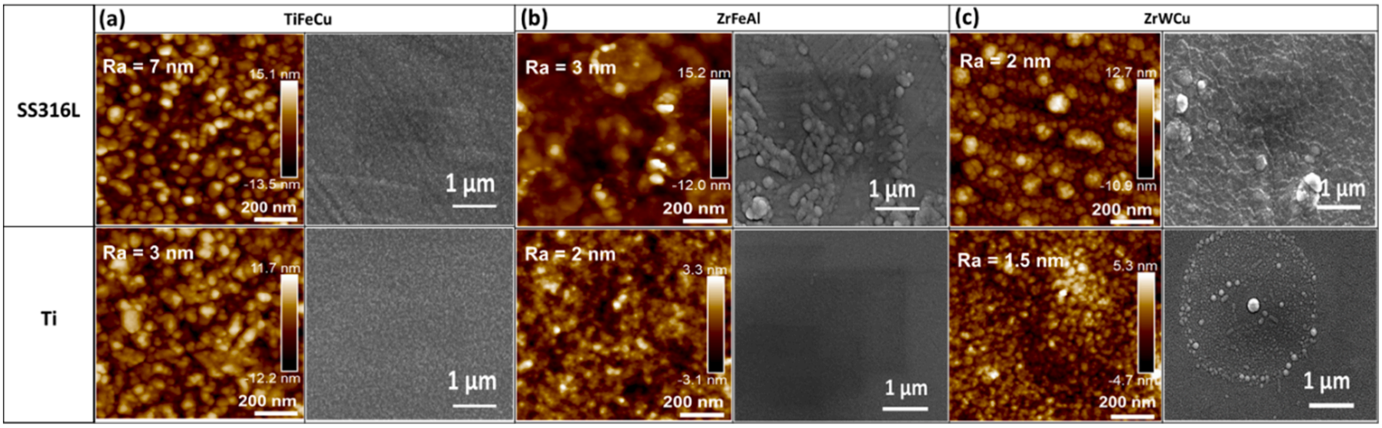

Fig. 4. AFM and FESEM micrographs of (a) Ti-Fe-Cu, (b) Zr-Fe-Al, and (c) Zr-W-Cu thin film metallic glass on SS316L and Ti substrates. Inset shows roughness (Ra) values of each film. .

Table 3
Young's modulus (E) and surface hardness (H) of the bare substrates (SS316L and Ti), and Ti- and Zr-based metallic glasses.

Sample	SS316L substrate		Ti substrate		Ref
	E (GPa)	*H* (GPa)	*E* (GPa)	*H* (GPa)	
Bare	210	1.7 – 2.2	120	3.3 – 3.7	[62–67]
$Ti_{47}Fe_{41}Cu_{12}$	74.7 ± 8.4	2.9 ± 1.0	75.0 ± 8.3	0.7 ± 0.8	This work
$Zr_{71}Fe_3Al_{26}$	93.6 ± 10.4	4.3 ± 1.2	93.8 ± 5.1	3.4 ± 0.5	This work
$Zr_{58}W_{31}Cu_{11}$	90.8 ± 9.6	1.8 ± 0.9	89.6 ± 4.9	1.3 ± 0.4	This work
$Ti_{40}Zr_{10}Cu_{36}Pd_{14}$	80	-	80	5.5	[64]
$Zr_{46}Cu_{46}Al_8$	96.4	–	96.4	–	[70]
$Zr_{50}Cu_{50}$	84	–	84	–	[71]
$Zr_{42}Cu_{42}Al_7Y_5$	84.6	–	84.6	–	[72]

Table 4
Critical values of *Lf* (i, ii, and iii) with the corresponding *dL* for the individual ramping *Nf* (2000, 3000, and 5000 μN) scratch track on the bare substrates and PTFMG-coated substrates as reference for substrate contact/effect.

Sample	Notations *Nf* (μN)	SS316L			Ti		
		2000 i	3000 ii	5000 iii	2000 i	3000 ii	5000 iii
Bare subtrate	*Lf* (μN)	778	1226	2554	687	903	3014
	dL (μm)	6.6	9.2	8.6	7.2	9.5	8.3
TiFeCu-coated	*Lf* (μN)	770	317	1921	800	1718	2629
	dL (μm)	9.4	9.8	8.9	9.6	9.1	8.5
ZrFeAl-coated	*Lf* (μN)	471	813	624	629	1349	2978
	dL (μm)	9.6	9.4	4.1	9.5	9.1	8.3
ZrWCu-coated	*Lf* (μN)	612	1065	2153	471	778	2261
	dL (μm)	9.4	9.2	8.7	9.7	9.6	8.6

Zr-Fe-Al PTFMG from the SS316L substrate at adhesive strength of 624 μN occurred. This low adhesive strength may be due to soft substrate effect of SS316L as reported for Zr-Cu-Al-Ni thin film MG-coated SS316L elsewhere [77–79]. Moreover , substrate effect may not be the only reason for the low adhesive strength of the Zr-Fe-Al PTFMG as the very small amount of Fe and higher Al (glue atoms) in the stoichiometry ($Zr_{71}Fe_3Al_{26}$) could have an effect [39,40]. Consequently, this weak adhesion observed for Zr-Fe-Al PTFMG on SS316L can be attributed due to the softer substrate and stoichiometric ratio of the glass forming elements. More research would be conducted to observe the effect of stoichiometric ratio on the adhesive strength of the Zr-Fe-Al PTFMG admixture on SS316L substrate.

In contrast, the *Lf* of Zr-Fe-Al on Ti substrate is consistent and progressive up to 2978 μN. The substrate was not reached with reference to Table 4 (Zr-Fe-Al-coated Ti *Lf* 2978 μN, *dL* 8.3 μm compared to bare Ti *Lf* 3014 μN, *dL*8.3 μm), hence no burst. This corresponds to the strong adhesion of Zr-based thin film MGs on hard substrate as reported by Marimuthu et al. [77]. Therefore, Zr-Fe-Al appears to have stronger adhesion on Ti substrate than SS316L due to higher substrate hardness (3.7 GPa vs 2.2 GPa), respectively [65–67].

Fig. 8 represents the *Lf* patterns (tracks with corresponding graphs) of nano-scratched Zr-W-Cu PTFMG on SS316L and Ti substrates for *Nf* 2000, 3000, and 5000 μN. The film exhibits excellent adhesion and fracture toughness on both substrates as no crack, burst or delamination was observed. Although a drop in *Lf* is observed at *dL* 7.7 μm on SS316L substrate, film delamination and breakage did not occur. This might have resulted from surface roughness as encircled in the FESEM image. Moreover, the small shear-band spacing of Zr-W-Cu PTFMG on SS316L substrate depicts better tribological properties (higher shear and wear resistance), thus, good film plasticity as compared to previous studies [18,80]. This is also substantiated by the higher *Lf* 2159 μN compared to $Zr_{50}Cu_{30}Al_{10}Ni_{10}$ (1900 μN), $Zr_{50}Cu_{35}Al_7Nb_5Pd_3$ (1806 μN) and $Zr_{55}Cu_{30}Al_7Nb_5Pd_3$ (1664 μN) [18,80].

On the other hand, Zr-W-Cu PTFMG on Ti substrate seems more ductile as the eroded material follows a malleable manner (folded pattern to the side and front without breakage). A close examination of the scratch tracks reveals ductile deformation due to the shear bands and dominant smooth interior scratch patterns [81].The substrate was not reached at any of the scratch track on film with reference to Table 4 which further suggests great wear, fracture, and shear resistance with peak *Lf* 2273 μN compared to other Zr-based thin film MGs. This is a resultant effect of dense atom packing and the polymorphic phase of Zr-W-Cu thin film MG on both substrates. This interesting tribological properties of Zr-W-Cu PTFMG on SS316L and Ti substrates show a great potential Zr-based thin film MG for sustainable coating.

Table 5 shows the adhesive strength (peak *Lf*s for *Nf* 5000 μN) and coefficient of friction (COF) of the co-sputtered PTFMGs on the individual substrates. Apparently, the thin films are stronger on Ti substrate as compared to SS316L. The COF was obtained as a function of the peak *Lf* (iii) ratio to the corresponding *Nf*. The COF recorded for the individual Ti and Zr-based thin film MGs is relatively low (< 0.6) and closely matched with earlier nano-scratch studies for Ti- and Zr-based thin film MGs (see Table 5).Since the tip geometry (radius 150 nm) can be expanded to 200 nm while in action [82], it can be said that the PTFMGs exhibited high strength (i.e. large *dL*) and fracture toughness (i.e. high *Lf*). The elastic recovery characterises this after deformation/expansion (in length as shown by the arrows on the FESEM images) and resistance

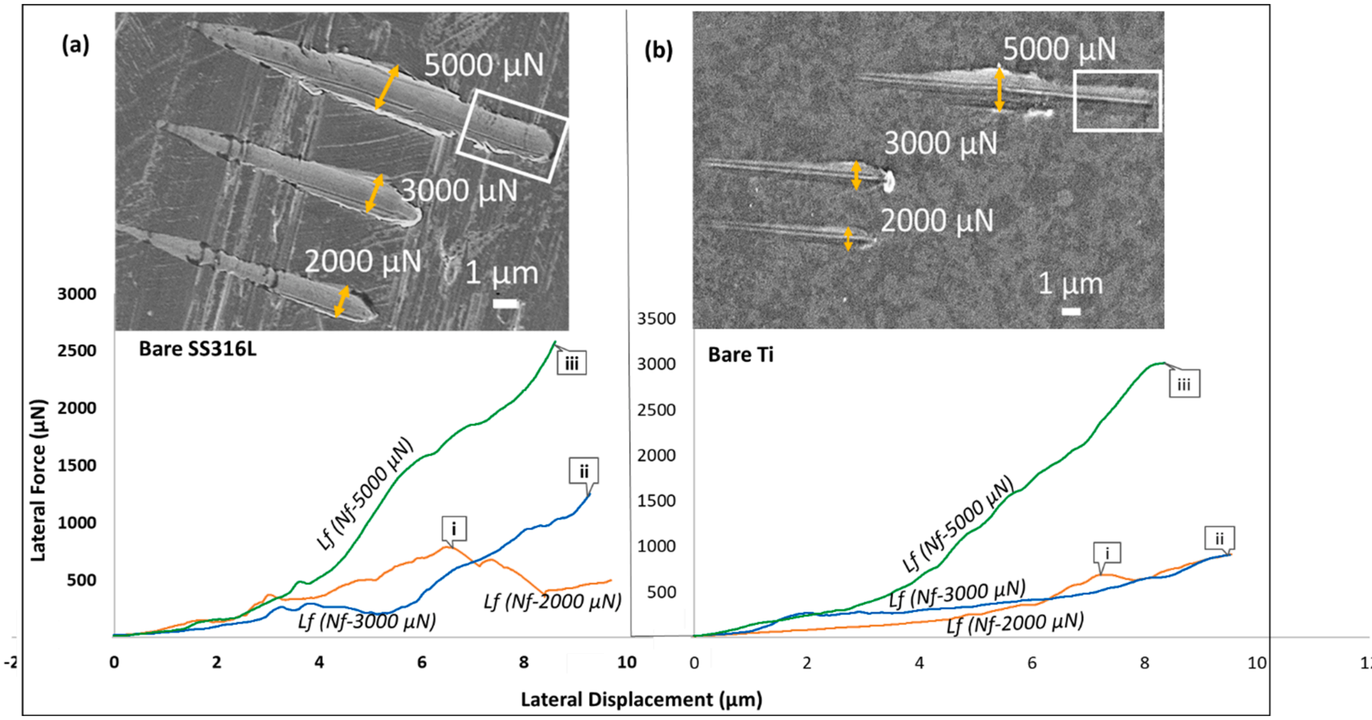

Fig. 5. Nano-scratch patterns: lateral force (*Lf*) for individual ramping normal force (*Nf*) on (a) bare SS316L and (b) bare Ti substrate.

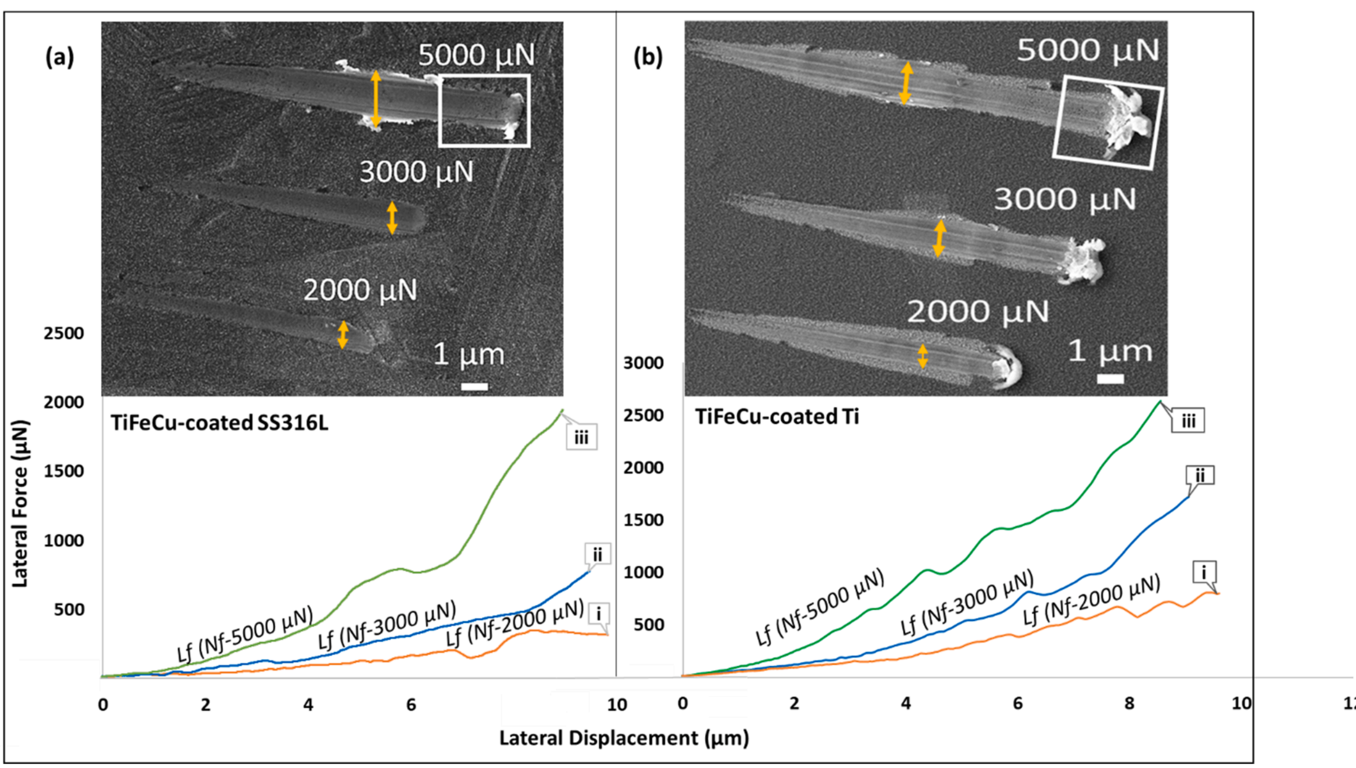

Fig. 6. Nano-scratch patterns: lateral force (*Lf*) for individual ramping normal force (*Nf*) for Ti-Fe-Cu PTFMG on (a) SS316L and (b) Ti Substrate.

to depth penetration without failure of the films by the tip with respect to *dL*.

Overall, less material was scratched off PTFMG-coated Ti compared to PTFMG-coated SS316L substrate. This shows that the film's wear resistance on Ti substrate is excellent and higher than on SS316L substrate and this can be attributed due to the higher hardness and low roughness of the substrate. These tribological properties, avail great benefits as sustainable surface coating for Ti and SS316L substrates with respect to industrial and biomedical applications.

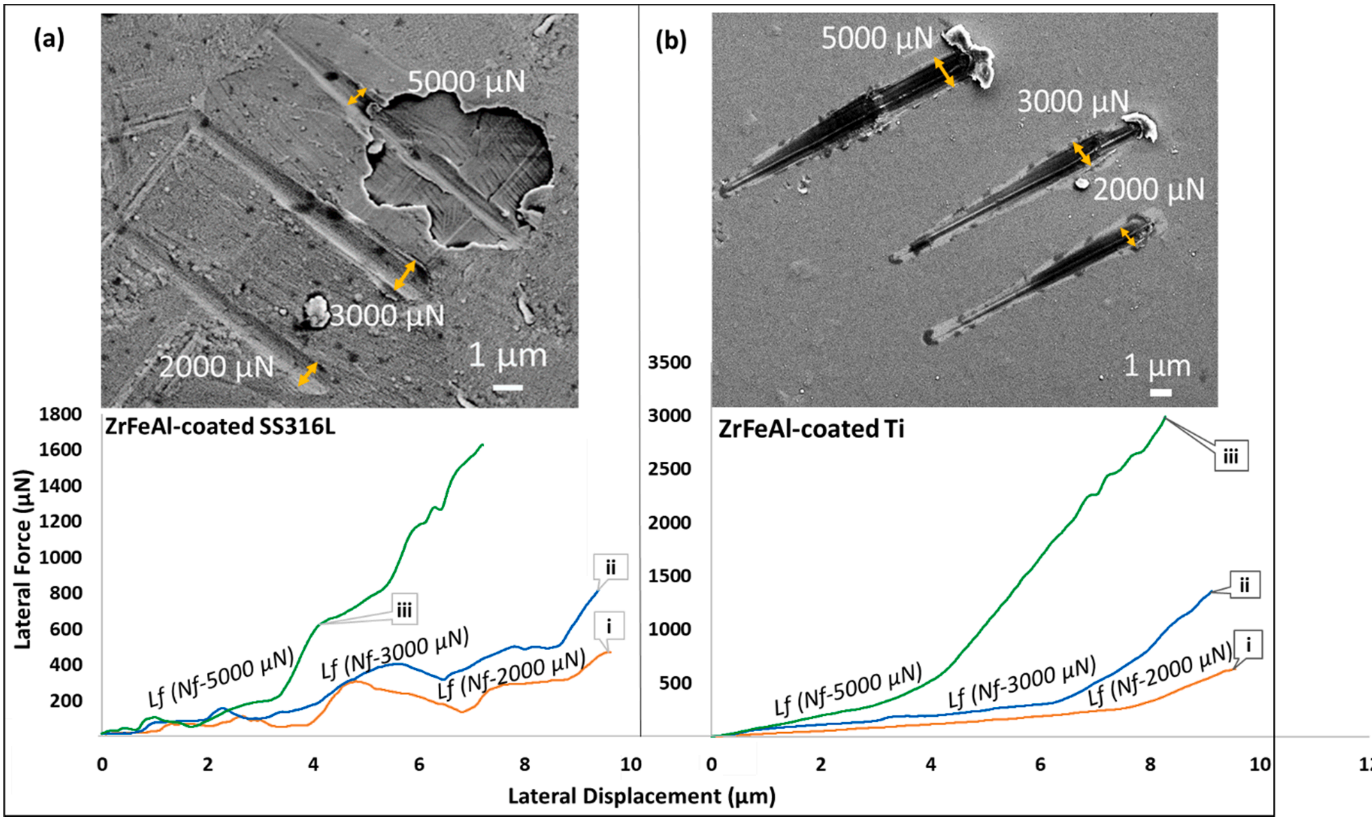

Fig. 7. Nano-scratch patterns: lateral force (*Lf*) for individual ramping normal force (*Nf*) for as-deposited Zr-Fe-Al PTFMG on (a) SS316L and (b) Ti Substrate.

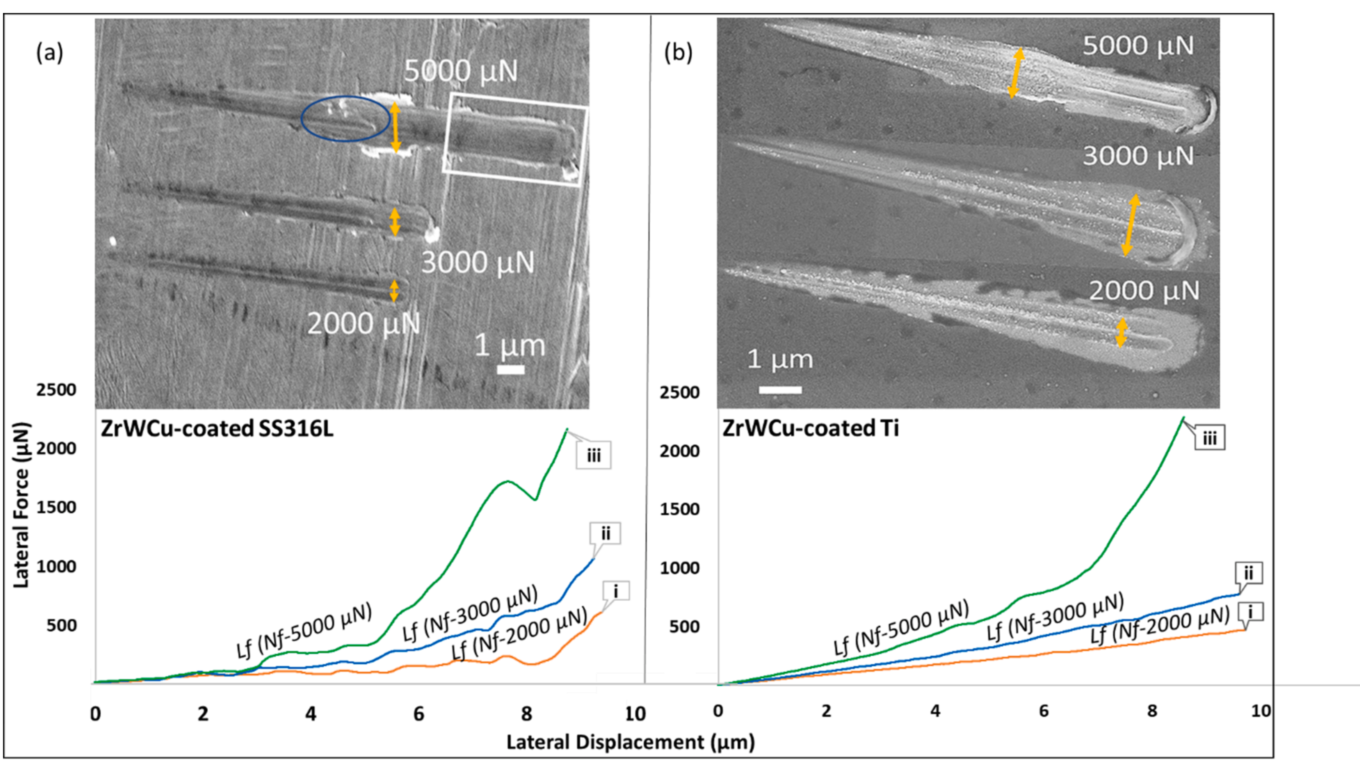

Fig. 8. Nano-scratch patterns: lateral force (*Lf*) for individual ramping normal force (*Nf*) for as-deposited Zr-W-Cu PTFMG on (a) SS316L and (b) Ti Substrate.

4. Conclusions

The need for mechanically robust functional materials is the motivation behind surface engineering/coating which avails the benefit of sustainability. $Ti_{47}Fe_{41}Cu_{12}$, $Zr_{71}Fe_3Al_{26}$, and $Zr_{58}W_{31}Cu_{11}$ PTFMGs (< 300 nm thick) were developed on medical grade SS316L and Ti

Table 5
Film Adhesive strength (FAS) and coefficient of friction (COF) of the PTFMG on SS316L and Ti substrates and COF of Ti-and Zr-based thin film MGs. COF of Zr-Fe-Al on SS316L was not calculated as delamination occurred before the reaching the maximum scratch distance (dL).

Sample	FAS (μN)/(MPa)		COF		Ref
	SS316L	Ti	SS316L	Ti	
Ti-Fe-Cu PTFMG	1921	2629	0.38	0.52	This work
Zr-Fe-Al PTFMG	624	2978	–	0.59	This work
Zr-W-Cu PTFMG	2159	2273	0.43	0.45	This work
Zr-based MGs	–	–	0.37–0.53		[83]
Ti-based MGs	–	–	0.19–0.67		[84,85]

substrates by co-sputtering of selected glass forming elements having incompatible crystal structures (HCP, BCC, FCC). The surface and nanomechanical properties including surface morphology, microstructure, mechanical, and tribological properties of the films were investigated. Homogeneous nanostructured films with low surface roughness of less than 10 nm, and no visible cracks were obtained. The unique combination of crystal structures of the constituents produces polymorphic phase (> 50% amorphous) thin films, which fosters nanomechanical properties with high strength, stiffness, and fracture toughness. The adhesion of all the films on both substrates was excellent, with film adhesive/tensile strength over 2000 μN/MPa except for Zr-Fe-Al (624 μN/MPa) on SS316L substrate. The imbalance amount of Fe and Al in the film is suggested as the cause of low adhesion strength of $Zr_{71}Fe_3Al_{26}$ film on the SS316L substrate. The PTFMGs have relatively low coefficient of friction (< 0.6) which is desirable property for minimising wear. It is concluded that the polymorphic properties of metallic glass thin films have shown strong nanomechanical and tribological properties suitable for applications requiring mechanically robust functional materials. Subsequent study will be performed to examine the biocorrosion and bactericidal efficacy of these polymorphic nanostructured thin film metallic glass coatings for biomedical application.

Funding

This work was funded by QUT MMPE ECRSEED grant (323100–0520/07, 2021).

Declaration of Competing Interest

The authors declare the following financial interests/personal relationships which may be considered as potential competing interests:

Tuquabo Tesfamichael, PHD reports financial support was provided by Queensland University of Technology.

Data availability

Data will be made available on request.

Acknowledgement

This work pertains to PHD program with Queensland University of Technology (QUT) Brisbane, Australia. Authors would like to acknowledge staffs of the Central Analytical Research Facility (CARF) QUT for their assistance through the research and analysis.

Supplementary materials

Supplementary material associated with this article can be found, in the online version, at doi:10.1016/j.surfin.2023.103090.

References

[1] S.W.M.A.I. Senevirathne, J. Hasan, A. Mathew, M. Woodruff, P.K.D.V. Yarlagadda, Bactericidal efficiency of micro- and nanostructured surfaces: a critical perspective, RSC Adv. 11 (3) (2021) 1883–1900, https://doi.org/10.1039/D0RA08878A.
[2] D.T. Elliott, R.J. Wiggins, R. Dua, Bioinspired antibacterial surface for orthopedic and dental implants, J. Biomed. Mater. Res. Part B Appl. Biomater. 109 (7) (2021) 973–981, https://doi.org/10.1002/jbm.b.34762.
[3] Y. Zhang, J.L. Li, T. Cai, Z.L. Cheng, X. Li, T.S. Chung, Sulfonated hyperbranched polyglycerol grafted membranes with antifouling properties for sustainable osmotic power generation using municipal wastewater, J. Memb. Sci. 563 (2018) 521–530, https://doi.org/10.1016/j.memsci.2018.05.017.
[4] D. Pavithra, M. Doble, Biofilm formation, bacterial adhesion and host response on polymeric implants-issues and prevention, Biomed. Mater. 3 (3) (2008), 034003, https://doi.org/10.1088/1748-6041/3/3/034003.
[5] E.P. Ivanova, et al., Natural bactericidal surfaces: mechanical rupture of pseudomonas aeruginosa cells by cicada wings, Small 8 (16) (2012) 2489–2494, https://doi.org/10.1002/smll.201200528.
[6] Y.T. Cheng, D.E. Rodak, C.A. Wong, C.A. Hayden, Effects of micro- and nano-structures on the self-cleaning behaviour of lotus leaves, Nanotechnology 17 (5) (2006) 1359–1362, https://doi.org/10.1088/0957-4484/17/5/032.
[7] P.M. Tsimbouri, et al., Osteogenic and bactericidal surfaces from hydrothermal titania nanowires on titanium substrates, Sci. Rep. 6 (1) (2016), https://doi.org/10.1038/srep36857.
[8] D.P. Linklater, V.A. Baulin, S. Juodkazis, R.J. Crawford, P. Stoodley, E.P. Ivanova, Mechano-bactericidal actions of nanostructured surfaces, Nat. Rev. Microbiol. 19 (1) (2021), https://doi.org/10.1038/s41579-020-0414-z.
[9] E.P. Ivanova, et al., The multi-faceted mechano-bactericidal mechanism of nanostructured surfaces, Proc. Nat. Acad. Sci. 117 (23) (2020) 12598–12605, https://doi.org/10.1073/pnas.1916680117.
[10] J.D. Bernal, J. Mason, Packing of spheres: co-ordination of randomly packed spheres, Nature 188 (4754) (1960), https://doi.org/10.1038/188910a0.
[11] A. Inoue, Stabilization of metallic supercooled liquid and bulk amorphous alloys, Acta Mater. 48 (1) (2000) 279–306, https://doi.org/10.1016/S1359-6454(99)00300-6.
[12] M. Telford, The case for bulk metallic glass, Mater. Today 7 (3) (2004) 36–43, https://doi.org/10.1016/S1369-7021(04)00124-5.
[13] D.V. Louzguine-Luzgin, A. Inoue, K.H.J. Buschow, Chapter three - bulk metallic glasses: formation, structure, properties, and applications. Handbook of Magnetic Materials, Elsevier, 2013, pp. 131–171, https://doi.org/10.1016/B978-0-444-59593-5.00003-9.
[14] H.F. Li, Y.F. Zheng, Recent advances in bulk metallic glasses for biomedical applications, Acta Biomater. 36 (2016) 1–20, https://doi.org/10.1016/j.actbio.2016.03.047.
[15] C.L. Qiu, et al., A novel Ni-free Zr-based bulk metallic glass with enhanced plasticity and good biocompatibility, Scr Mater. 55 (7) (2006) 605–608, https://doi.org/10.1016/j.scriptamat.2006.06.018.
[16] F.X. Qin, X.M. Wang, G.Q. Xie, A. Inoue, Distinct plastic strain of Ni-free Ti-Zr-Cu-Pd-Nb bulk metallic glasses with potential for biomedical applications, Intermetallics 16 (8) (2008) 1026–1030, https://doi.org/10.1016/j.intermet.2008.05.004.
[17] M.E. Launey, D.C. Hofmann, J.Y. Suh, H. Kozachkov, W.L. Johnson, R.O. Ritchie, Fracture toughness and crack-resistance curve behavior in metallic glass-matrix composites, Appl. Phys. Lett. 94 (24) (2009), 241910, https://doi.org/10.1063/1.3156026.
[18] K. Imai, X. Zhou, and X. Liu, "Application of Zr and Ti-based bulk metallic glasses for orthopaedic and dental device materials," Metals, vol. 10, no. 2, p. 203, Feb. 2020, doi: 10.3390/met10020203.
[19] L. Tian, X.L. Wang, Z.W. Shan, Mechanical Behavior of Micronanoscaled Metallic Glasses, Mater. Res. Lett. 4 (2) (2016) 63–74, https://doi.org/10.1080/21663831.2015.1124298.
[20] W.P. Wu, D. Şopu, X. Yuan, J. Eckert, Aspect ratio-dependent nanoindentation behavior of Cu64Zr36 metallic glass nanopillars investigated by molecular dynamics simulations, J. Appl. Phys. 128 (8) (2020), 084303, https://doi.org/10.1063/5.0014263.
[21] J.C. Ye, J. Lu, C.T. Liu, Q. Wang, Y. Yang, Atomistic free-volume zones and inelastic deformation of metallic glasses, Nat. Mater. 9 (8) (2010), https://doi.org/10.1038/nmat2802.
[22] C.Q. Chen, Y.T. Pei, O. Kuzmin, Z.F. Zhang, E. Ma, J. Th. M. De Hosson, Intrinsic size effects in the mechanical response of taper-free nanopillars of metallic glass, Phys. Rev. B 83 (18) (2011), 180201, https://doi.org/10.1103/PhysRevB.83.180201.
[23] P.S. Chen, H.W. Chen, J.G. Duh, J.W. Lee, J.S.C. Jang, Characterization of mechanical properties and adhesion of Ta–Zr–Cu–Al–Ag thin film metallic glasses, Surf. Coat. Technol. 231 (2013) 332–336, https://doi.org/10.1016/j.surfcoat.2012.03.087.
[24] B. Subramanian, S. Maruthamuthu, S.T. Rajan, Biocompatibility evaluation of sputtered zirconium-based thin film metallic glass-coated steels, Int J Nanomedicine 10 (2015) 17–29, https://doi.org/10.2147/IJN.S79977.
[25] A. Inoue, X. Wang, W. Zhang, Developments and applications of bulk metallic glasses, Rev.Adv.Mater.Sci 18 (2008) 1–9.
[26] "Amorphous Alloy Surpasses Steel and Titanium | NASA Spinoff." https://spinoff.nasa.gov/Spinoff2004/ch_7.html (accessed May 28, 2022).
[27] Y. Fu, H. Du, W. Huang, S. Zhang, M. Hu, TiNi-based thin films in MEMS applications: a review, Sens. Actuators A Phys. 112 (2) (2004) 395–408, https://doi.org/10.1016/j.sna.2004.02.019.

[28] S.T. Rajan, A. Arockiarajan, Thin film metallic glasses for bioimplants and surgical tools: a review, J. Alloys Compd. 876 (2021), 159939, https://doi.org/10.1016/j.jallcom.2021.159939.
[29] G. Greczynski, L. Hultman, X-ray photoelectron spectroscopy: towards reliable binding energy referencing, Prog. Mater. Sci. 107 (2020), 100591, https://doi.org/10.1016/j.pmatsci.2019.100591.
[30] Y.F. Gao, H.T. Xu, W.C. Oliver, G.M. Pharr, Effective elastic modulus of film-on-substrate systems under normal and tangential contact, J. Mech. Phys. Solids 56 (2) (2008) 402–416, https://doi.org/10.1016/j.jmps.2007.05.015.
[31] "A review on nano - indentation of thin polymeric films," *Int. J. Eng. Res.*, vol. 8, no. 03.
[32] "(17) (PDF) Determination of material properties of thin films and coatings using indentation tests: a review." https://www.researchgate.net/publication/318474336_Determination_of_material_properties_of_thin_films_and_coatings_using_indentation_tests_a_review (accessed Aug. 23, 2022).
[33] 14:00-17:00, "ISO 14577-4:2016," *ISO*. https://www.iso.org/cms/render/live/en/sites/isoorg/contents/data/standard/06/18/61823.html (accessed Aug. 23, 2022).
[34] F.X. Liu, Y. Gao, P. Liaw, Rate-Dependent Deformation Behavior of Zr-Based Metallic-Glass Coatings Examined by Nanoindentation, Metallurgical and Materials Transactions A 39 (2008) 1862–1867, https://doi.org/10.1007/s11661-007-9399-8.
[35] "The influence of hydrogen on the chemical, mechanical, optical/electronic, and electrical transport properties of amorphous hydrogenated boron carbide: J. Appl. Phys.: Vol 118, No 3." https://aip.scitation.org/doi/10.1063/1.4927037 (accessed Aug. 23, 2022).
[36] N. Tayebi, T. Conry, A. Polycarpou, Determination of hardness from nanoscratch experiments: corrections for interfacial shear stress and elastic recovery, J. Mater. Res. 18 (2003) 2150–2162, https://doi.org/10.1557/JMR.2003.0301.
[37] T.P. Hsiao, Y.C. Yang, J.W. Lee, C.L. Li, J.P. Chu, The microstructure and mechanical properties of nitrogen and boron contained ZrCuAlNi thin film metallic glass composites, Surf. Coat. Technol. 237 (2013) 276–283, https://doi.org/10.1016/j.surfcoat.2013.09.015.
[38] J. Shen, Q. Chen, J. Sun, H. Fan, G. Wang, Exceptionally high glass-forming ability of an FeCoCrMoCBY alloy, Appl. Phys. Lett. 86 (15) (2005), 151907, https://doi.org/10.1063/1.1897426.
[39] Z.R. Wang, J.B. Qiang, Y.M. Wang, Q. Wang, D.D. Dong, C. Dong, Composition design procedures of Ti-based bulk metallic glasses using the cluster-plus-glue-atom model, Acta Mater. 111 (2016) 366–376, https://doi.org/10.1016/j.actamat.2016.03.072.
[40] G.J. Naz, D. Dong, Y. Geng, Y. Wang, C. Dong, Composition formulas of Fe-based transition metals-metalloid bulk metallic glasses derived from dual-cluster model of binary eutectics, Sci. Rep. 7 (1) (2017) 9150, https://doi.org/10.1038/s41598-017-09100-9.
[41] S. Zheng, et al., Implication of surface properties, bacterial motility, and hydrodynamic conditions on bacterial surface sensing and their initial adhesion, Front. Bioeng. Biotechnol. 9 (2021). Accessed: Oct. 07, 2022. Available: https://www.frontiersin.org/articles/10.3389/fbioe.2021.643722.
[42] V.K. Truong, et al., The influence of nano-scale surface roughness on bacterial adhesion to ultrafine-grained titanium, Biomaterials 31 (13) (2010) 3674–3683, https://doi.org/10.1016/j.biomaterials.2010.01.071.
[43] W.L. Johnson, K. Samwer, A universal criterion for plastic yielding of metallic glasses with a (T/Tg)2/3 temperature dependence, Phys. Rev. Lett. 95 (19) (2005), 195501, https://doi.org/10.1103/PhysRevLett.95.195501.
[44] W. Tang, X. Weng, L. Deng, K. Xu, J. Lu, Nano-scratch experiments of Au/NiCr multi-layered films for microwave integrated circuits, Surf. Coat. Technol. 201 (9) (2007) 5664–5666, https://doi.org/10.1016/j.surfcoat.2006.07.054.
[45] D.A. Tallarico, A.L. Gobbi, P.I. Paulin Filho, M.E.H. Maia da Costa, P.A.P. Nascente, Growth and surface characterization of TiNbZr thin films deposited by magnetron sputtering for biomedical applications, Mater. Sci. Eng. C 43 (2014) 45–49, https://doi.org/10.1016/j.msec.2014.07.013.
[46] F.A. El Diwany, T. Al Najjar, N.K. Allam, E.N. El Sawy, Tungsten oxide/fullerene-based nanocomposites as electrocatalysts and parasitic reactions inhibitors for VO2+/VO2+ in mixed-acids, Sci. Rep. 12 (1) (2022), https://doi.org/10.1038/s41598-022-18561-6.
[47] "Tungsten | XPS Periodic Table - AU." https://www.thermofisher.com/au/en/home/materials-science/learning-center/periodic-table/transition-metal/tungsten.html (accessed Jun. 07, 2023).
[48] M.C. Biesinger, L.W.M. Lau, A.R. Gerson, R. St. C. Smart, Resolving surface chemical states in XPS analysis of first row transition metals, oxides and hydroxides: *sc*, Ti, V, Cu and Zn, Appl. Surf. Sci. 257 (3) (2010) 887–898, https://doi.org/10.1016/j.apsusc.2010.07.086.
[49] N.B. Viorel, H.F. Chicinas, T. Marinca, O. Isnard, O. Pana, I. Chicinas, Amorphisation of Fe-based alloy via wet mechanical alloying assisted by PCA decomposition, Mater. Chem. Phys. 183 (2016) 83–92, https://doi.org/10.1016/j.matchemphys.2016.08.005.
[50] Y. Wang, L.L. Wang, C.Q. Sun, The 2p3/2 binding energy shift of Fe surface and Fe nanoparticles, Chem. Phys. Lett. 480 (4) (2009) 243–246, https://doi.org/10.1016/j.cplett.2009.09.017.
[51] M. Hierro-Oliva, A.M. Gallardo-Moreno, M.L. González-Martín, XPS analysis of Ti_6Al_4V oxidation under UHV conditions, Metall. Mat. Trans. A 45 (13) (2014) 6285–6290, https://doi.org/10.1007/s11661-014-2570-0.
[52] S. Komornicki, M. Radecka, P. Sobaś, Structural properties of TiO_2 –WO_3 thin films prepared by r.f. sputtering, J. Mater. Sci.Mater. Electron. 15 (2004) 527–531, https://doi.org/10.1023/B:JMSE.0000032587.22033.d0.
[53] W. Xie, R. Li, S.Q. Xu, Enhanced photocatalytic activity of Se-doped TiO_2 under visible light irradiation, Sci. Rep. 8 (2018), https://doi.org/10.1038/s41598-018-27135-4.
[54] Y. Nishihara, et al., Isothermal compression of face-centered cubic iron, Am. Mineralog. 97 (8–9) (2012) 1417–1420, https://doi.org/10.2138/am.2012.3958.
[55] V.N. Eremenko, T. Ya Velikanova, S.V. Shabanova, G.V. Samsonov, The phase diagram of the system titanium—molybdenum—carbon. Refractory Carbides, Springer US, New York, NY, 1974, pp. 143–155, https://doi.org/10.1007/978-1-4684-8598-1_16. Studies in Soviet Science.
[56] V.A. Yartys, H. Fjellvåg, B.C. Hauback, A.B. Riabov, M.H. Sørby, Neutron diffraction studies of Zr-containing intermetallic hydrides with ordered hydrogen sublattice. II. Orthorhombic $Zr_3FeD_{6.7}$ with filled Re_3B-type structure, J. Alloys Compd. 278 (1) (1998) 252–259, https://doi.org/10.1016/S0925-8388(98)00592-1.
[57] Y. Su, J. Yan, P. Lu, J. Su, Thermodynamic analysis and experimental research on Li intercalation reactions of the intermetallic compound Al_2Cu, Solid State Ion. 177 (5) (2006) 507–513, https://doi.org/10.1016/j.ssi.2005.12.007.
[58] J.S. Shah, M.E. Straumanis, Thermal expansion of tungsten at low temperatures, J. Appl. Phys. 42 (9) (1971) 3288–3289, https://doi.org/10.1063/1.1660727.
[59] H.S. Chou, J.C. Huang, L.W. Chang, T.G. Nieh, Structural relaxation and nanoindentation response in Zr–Cu–Ti amorphous thin films, Appl. Phys. Lett. 93 (19) (2008), 191901, https://doi.org/10.1063/1.2999592.
[60] J.R. Greer, J. Th. M. De Hosson, Plasticity in small-sized metallic systems: intrinsic versus extrinsic size effect, Prog. Mater. Sci. 56 (6) (2011) 654–724, https://doi.org/10.1016/j.pmatsci.2011.01.005.
[61] J. Gong, H. Miao, Z. Peng, L. Qi, Effect of peak load on the determination of hardness and Young's modulus of hot-pressed Si_3N_4 by nanoindentation, Mater. Sci. Eng. A 354 (1) (2003) 140–145, https://doi.org/10.1016/S0921-5093(02)00940-1.
[62] M. Rossi, F. Pierron, M. Štamborská, F. Šimčák, C.E. Ventura, W.C. Crone, C. Furlong, Identification of the anisotropic plastic behaviour of sheet metals at large strains. Experimental and Applied Mechanics, Volume 4, Springer New York, New York, NY, 2013, pp. 229–235, https://doi.org/10.1007/978-1-4614-4226-4_27. Conference Proceedings of the Society for Experimental Mechanics Series.
[63] "Titanium Properties, " Kyocera SGS Europe. https://kyocera-sgstool.co.uk/titanium-resources/titanium-information-everything-you-need-to-know/titanium-properties/ (accessed Jun. 03, 2023).
[64] A. Liens, et al., On the potential of bulk metallic glasses for dental implantology: case study on $Ti_{40}Zr_{10}Cu_{36}Pd_{14}$, Materials (Basel) 11 (2018) 249, https://doi.org/10.3390/ma11020249.
[65] "Properties: Stainless Steel - Grade 316 (UNS S31600)," *AZoM.com*. https://www.azom.com/properties.aspx?ArticleID=863 (accessed Oct. 12, 2022).
[66] "Properties: Titanium Alloys - Ti6Al4V Grade 5." https://www.azom.com/properties.aspx?ArticleID=1547 (accessed Oct. 12, 2022).
[67] J.L. Ke, C.H. Huang, Y.H. Chen, W.Y. Tsai, T.Y. Wei, J.C. Huang, In vitro biocompatibility response of Ti–Zr–Si thin film metallic glasses, Appl. Surf. Sci. 322 (2014) 41–46, https://doi.org/10.1016/j.apsusc.2014.09.204.
[68] T. Rajan S, A. Arockiarajan, Thin film metallic glasses for bioimplants and surgical tools: a review, J. Alloy. Compd. 876 (2021), 159939, https://doi.org/10.1016/j.jallcom.2021.159939.
[69] Q.K. Jiang, et al., Zr–(Cu,Ag)–Al bulk metallic glasses, Acta Mater. 56 (8) (2008) 1785–1796, https://doi.org/10.1016/j.actamat.2007.12.030.
[70] Juan Z., Guozheng K., and Wei R., "Review on the deformation behavior and constitutive equations of metallic glass matrix composites," lxxb, vol. 52, no. 2, pp. 318–332, Apr. 2020, doi: 10.6052/0459-1879-20-038.
[71] M. Apreutesei, et al., Microstructural, thermal and mechanical behavior of co-sputtered binary Zr–Cu thin film metallic glasses, Thin Solid Films 561 (2014) 53–59, https://doi.org/10.1016/j.tsf.2013.05.177.
[72] G.J. Fan, et al., Thermophysical and elastic properties of Cu50Zr50 and (Cu50Zr50)95Al5 bulk-metallic-glass-forming alloys, Appl. Phys. Lett. 89 (24) (2006), 241917, https://doi.org/10.1063/1.2408634.
[73] B.K. Gupta, B. Bhushan, Micromechanical properties of amorphous carbon coatings deposited by different deposition techniques, Thin Solid Films 270 (1) (1995) 391–398, https://doi.org/10.1016/0040-6090(95)06699-3.
[74] D.N. Allsopp, I.M. Hutchings, Micro-scale abrasion and scratch response of PVD coatings at elevated temperatures, Wear 251 (1) (2001) 1308–1314, https://doi.org/10.1016/S0043-1648(01)00755-4.
[75] F. Attar, T. Johannesson, Adhesion evaluation of thin ceramic coatings on tool steel using the scratch testing technique, Surf. Coat. Technol. 78 (1) (1996) 87–102, https://doi.org/10.1016/0257-8972(94)02396-4.
[76] F. Qin, Z. Dan, X. Wang, G. Xie, and A. Inoue, "Ti-based bulk metallic glasses for biomedical applications," 2011. doi: 10.5772/13437.
[77] K.P. Marimuthu, J. Han, U. Jeong, K. Lee, H. Lee, Study on tribological characteristics of Zr-based BMG via nanoscratch techniques, Wear vol. 486–487 (2021), 204067, https://doi.org/10.1016/j.wear.2021.204067.
[78] K.P. Marimuthu, U. Jeong, J. Han, G. Han, H. Lee, Influence of substrate type and film thickness on the failures of Zr-based thin-film metallic glass under nanoscratch, Wear 494–495 (2022), 204241, https://doi.org/10.1016/j.wear.2022.204241.
[79] C. Zhang, T. Hu, N. Zhang, Influence of Substrate Hardness on Coating-Substrate Adhesion, Adv. Mat. Res. 177 (2011) 148–150. 10.4028/www.scientific.net/AMR.177.148.
[80] G.Y. Wang, P.K. Liaw, Y. Yokoyama, A. Inoue, C.T. Liu, Fatigue behavior of Zr-based bulk-metallic glasses, Mater. Sci. Eng. A 494 (1) (2008) 314–323, https://doi.org/10.1016/j.msea.2008.04.034.

[81] G. Subhash, H. Zhang, Shear band patterns in metallic glasses under static indentation, dynamic indentation, and scratch processes, Metall. Mater. Trans. A 38 (12) (2007) 2936–2942, https://doi.org/10.1007/s11661-007-9315-2.
[82] P. Murugasen, Novel Analysis on the Influence of Tip Radius and Shape of the Nanoindenter on the Hardness of Materials, Procedia. Mater. Sci. 6 (2014) 1871–1878, https://doi.org/10.1016/j.mspro.2014.07.218.
[83] E. Fleury, S.M. Lee, H.S. Ahn, W.T. Kim, D.H. Kim, Tribological properties of bulk metallic glasses, Mater. Sci. Eng. A 375–377 (2004) 276–279, https://doi.org/10.1016/j.msea.2003.10.065.
[84] F. Cao, et al., Wear Behaviors of a Ti-Based Bulk Metallic Glass at Elevated Temperatures, Front. Mater. 8 (2021). Accessed: Jun. 03, 2023. Available: https://www.frontiersin.org/articles/10.3389/fmats.2021.695840.
[85] Y.X. Ye, C.Z. Liu, H. Wang, T.G. Nieh, Friction and wear behavior of a single-phase equiatomic TiZrHfNb high-entropy alloy studied using a nanoscratch technique, Acta Mater. 147 (2018) 78–89, https://doi.org/10.1016/j.actamat.2018.01.014.